Cimbri, D., Wang, J. and Wasige, E. (2022) Epitaxial Structure Simulation Study of $In_{0.53}Ga_{0.47}As$/AlAs Double-Barrier Resonant Tunnelling Diodes. In: 2022 Fifth IEEE International Workshop on Mobile Terahertz Systems (IWMTS), Duisburg, Germany, 04-06 Jul 2022, ISBN 9781665482752

(doi: 10.1109/IWMTS54901.2022.9832441)

Epitaxial Structure Simulation Study of $In_{0.53}Ga_{0.47}As$/AlAs Double-Barrier Resonant Tunnelling Diodes

Davide Cimbri[1]*, Jue Wang[1], and Edward Wasige[1]

[1]High-Frequency Electronics group, Division of Electronics and Nanoscale Engineering, James Watt School of Engineering,
University of Glasgow, G12 8LT, Glasgow, United Kingdom

*davide.cimbri@glasgow.ac.uk

***Abstract*—In this paper, we report about an epitaxial structure simulation study of $In_{0.53}Ga_{0.47}As$/AlAs double-barrier resonant tunneling diodes (RTD) employing Atlas TCAD quantum transport simulation software developed by SILVACO Inc., which is based on the non-equilibrium Green's function formalism. We analyse how epitaxial layers design impacts the heterostructure static current density-voltage characteristic, including barriers, quantum well (QW), and lightly-doped spacer layers, as well as the employment of a high-bandgap emitter region. Our analysis shows that, while barriers and QW thicknesses have a strong impact on the current density operation of the RTD device, accurate asymmetric spacers design can trade-off between the voltage span and relative position of its negative differential resistance region. This work will guide in optimising the RTD epitaxial structure in order to maximise its RF power performance at low-terahertz frequencies ($\sim$ 100$-$300 GHz).**

***Index Terms*—Resonant tunnelling diode, double-barrier quantum well, non-equilibrium Green's function, epitaxial structure design.**

I. INTRODUCTION

RESONANT tunnelling diodes (RTD) [1] are the fastest demonstrated solid-state semiconductor-based electronic devices operating at room temperature (RT), which makes them attractive for consumer-oriented terahertz (THz) (0.1$-$10 THz [2]) applications. Indeed, maximum oscillation frequencies f_{max} up to around 2 THz have been attained in indium phosphide (InP) technology [3], providing a milestone for the viability of next-generation ultra-high-speed wireless communications [4] [5]. In this context, accurate device epitaxial structure design optimisation is crucial to tailor both sources and detectors performance according to the operational requirements. However, this needs a clear and comprehensive understanding on how epitaxial structure parameters impact the electrical properties of the RTD device.

In this paper, we present an epitaxial structure simulation study of lattice-matched to InP indium gallium arsenide/aluminium arsenide ($In_{0.53}Ga_{0.47}As$/AlAs) double-barrier RTDs by making use of the approach we have demonstrated in [6], which is based on the Non-equilibrium Green's Function (NEGF) method implemented in SILVACO Inc. Atlas TCAD quantum transport simulation package. By tuning the parameters associated with epitaxial layers, including barriers, quantum well (QW), and lightly-doped spacer layers, we analysed the impact on the associated static current density-voltage (JV) characteristic in terms of peak current density J_p, peak voltage V_p, and valley-to-peak voltage difference $\Delta V = V_v - V_p$ of the negative differential resistance (NDR) region, which are the electrical quantities that can be accurately estimated with the current release of the software. A qualitative analysis of the valley current density J_v, peak-to-valley current density difference $\Delta J = J_p - J_v$, and peak-to-valley current ratio PVCR $= J_p/J_v$ in terms of both barriers and QW design was carried out based on the heterostructure transmission coefficient. The employment of a high-bandgap material at the emitter side was also studied.

II. EPITAXIAL STRUCTURE SIMULATION STUDY

To investigate the impact of epitaxial structure design parameters on the heterostructure static JV characteristic, an n-type intraband $In_{0.53}Ga_{0.47}As$/AlAs double-barrier reference epitaxial structure (RES) with symmetric geometry, which is depicted in Fig. 1, was adopted, and consisted of: barriers thickness t_b = 1.46 nm; QW thickness t_{qw} = 4.39 nm; emitter/collector undoped spacers thickness: 2 nm; emitter/collector lightly-doped spacers thickness $t_{e/c,ls}$ = 100 nm and doping level $N_{De/c,ls} = 2{\times}10^{17}$ cm^{-3}; emit-

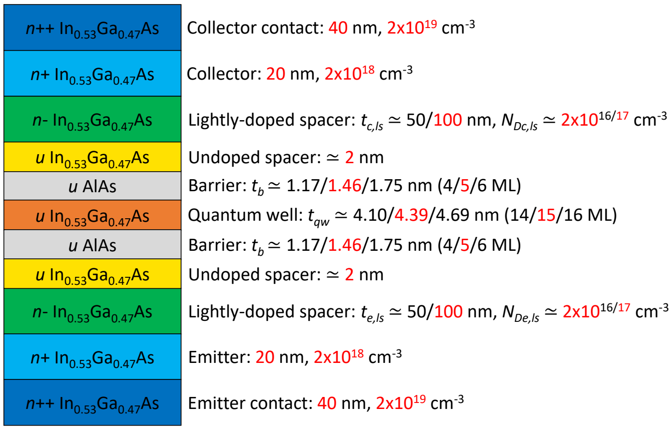

Fig. 1. Reference epitaxial structure (RES) and associated parameters (in red), including the whole set of simulation study parameters.

ter/collector thickness and doping level: 20 nm, 2×10^{18} cm^{-3}; emitter/collector heavily-doped contacts thickness and doping level: 40 nm, 2×10^{19} cm^{-3}. This choice was made based on reported epitaxial structures employed in oscillators operating below 300 GHz [7]. Parameters associated with barriers, QW, and lightly-doped spacers were tuned, as shown in Fig. 1, and simulation results compared and discussed. Forward bias (collector positively biased with respect to the emitter) and RT ($T = 300$ K) operation was assumed.

A. Barriers

The RES was simulated setting $t_b = 1.17$ nm, 1.46 nm, and 1.75 nm (4 ML, 5 ML, and 6 ML), where ML stands for monolayer (1 ML $\simeq$ 0.293 nm). The impact of t_b on the static JV characteristic was revealed in terms of current density, while the effect on voltages was negligible ($V_p \simeq 1.2$ V, $V_v \simeq 2.7$ V, and $\Delta V \simeq 1.5$ V). Simulation results are shown in Table I. As t_b increases, J_p decreases from $\simeq$ 656 kA/cm^2 with 4 ML to $\simeq$ 263 kA/cm^2 and $\simeq$ 101 kA/cm^2 with 5 ML and 6 ML, respectively, revealing an exponential trend $J_p \propto e^{-\alpha t_b}$ ($\alpha > 0$), which is explained by the drop of the full-width at half maximum (FWHM) Γ_1 of the heterostructure transmission coefficient T_{rtd} associated with the QW first quasi-bound state energy level E_1 resonant peak, which is shown in Fig. 2, which decreases from $\simeq$ 7.5 meV with 4 ML to $\simeq$ 2.9 meV and $\simeq$ 1.1 meV with 5 ML and 6 ML, respectively, increasing carrier confinement and narrowing the channel for electron tunnelling due to the lower associated available density of states. Although J_p increases by reducing t_b, the $T_{rtd}(E_2)$ resonant peak FWHM Γ_2 (where E_2 is the QW second quasi-bound state resonant level) increases more than Γ_1, from $\simeq$ 13.8 meV with 6 ML to $\simeq$ 25.1 meV and $\simeq$ 47.6 meV with 5 ML and 4 ML, respectively, where $d\Gamma_2/dt_b \gg d\Gamma_1/dt_b$ due to the weaker electron confinement, making the valley current density $J_v \propto e^{-\beta t_b}$ to rise more than J_p ($\beta \ll \alpha$).

In summary, the analysis showed that, while both J_p and the available current density $\Delta J = J_p - J_v$ increases reducing t_b, the peak-to-valley current ratio PVCR $= J_p/J_v$ drops, while V_p and ΔV are almost unchanged [8] [9].

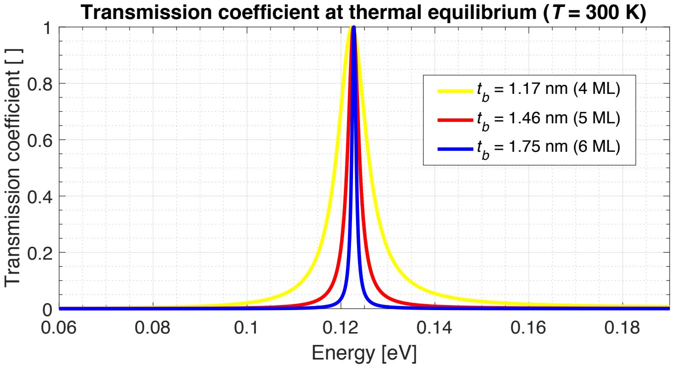

Fig. 2. Computed resonant peak associated with the QW first quasi-bound state energy level of the heterostructure transmission coefficient energy spectrum at RT and thermal equilibrium for different barriers thicknesses t_b.

TABLE I
SIMULATION RESULTS FOR DIFFERENT BARRIERS THICKNESSES

t_b [nm]	J_p [kA/cm^2]	V_p [V]	V_v [V]	ΔV [V]
1.17	656	1.2	2.7	1.5
1.46	263	1.2	2.7	1.5
1.75	101	1.2	2.7	1.5

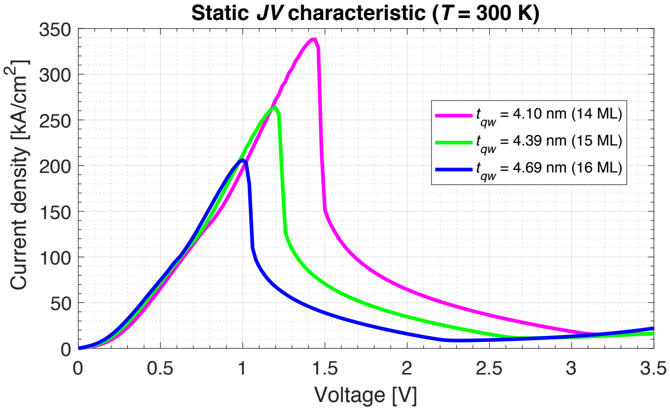

Fig. 3. Computed static JV characteristic at RT for different QW thicknesses t_{qw}.

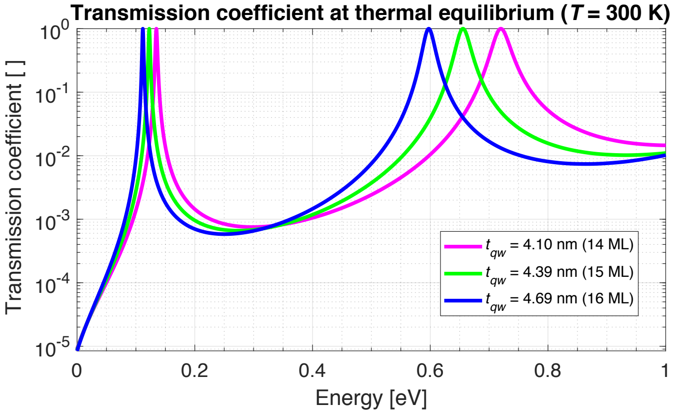

Fig. 4. Computed transmission coefficient energy spectrum at RT and thermal equilibrium for different QW thicknesses t_{qw}.

B. Quantum well

The RES was simulated setting $t_{qw} \simeq 4.10$ nm, $\simeq 4.39$ nm, and $\simeq 4.69$ nm (14 ML, 15 ML, and 16 ML). The computed static JV characteristics are shown in Fig. 3 and the associated values in Table II, which were $J_p \simeq 338$ kA/cm^2, $V_p \simeq 1.44$ V, and $\Delta V \simeq 1.78$ V with 14 ML, $J_p \simeq 263$ kA/cm^2, $V_p \simeq 1.20$ V, and $\Delta V \simeq 1.54$ V with 15 ML, and $J_p \simeq 206$ kA/cm^2, $V_p \simeq 1.00$ V, and $\Delta V \simeq 1.32$ V with 16 ML.

To compare and explain the results, the T_{rtd} of the heterostructures at RT was computed and analysed, which is shown in Fig. 4. Thermal equilibrium conditions were assumed to simplify the treatment. The increase in J_p and V_p with QW shrinking is

TABLE II
SIMULATION RESULTS FOR DIFFERENT QW THICKNESSES

t_{qw} [nm]	J_p [kA/cm^2]	V_p [V]	V_v [V]	ΔV [V]
4.10	338	1.44	3.22	1.78
4.39	263	1.20	2.74	1.54
4.69	206	1.00	2.32	1.32

explained by the rise of E_1, which increases from $\simeq$ 112 meV with 16 ML to $\simeq$ 123 meV ($\Delta E_1 \simeq$ 11 meV) and $\simeq$ 135 meV ($\Delta E_1 \simeq$ 23 meV) with 15 ML and 14 ML, respectively, and by the broadening of E_1 caused by the weaker wave-function confinement, where Γ_1 increases from $\simeq$ 2.5 meV with 16 ML to $\simeq$ 2.9 meV and $\simeq$ 3.3 meV with 15 ML and 14 ML, respectively. At the same time, E_2 rises more than E_1, which shifts from $\simeq$ 597 meV with 16 ML to $\simeq$ 656 meV ($\Delta E_2 \simeq$ 59 meV) and $\simeq$ 720 meV ($\Delta E_2 \simeq$ 123 meV) with 15 ML and 14 ML, respectively. This makes V_v to shift more than V_p ($V_v \simeq$ 2.32 V, $\simeq$ 2.74 V, and $\simeq$ 3.22 V with 16 ML, 15 ML, and 14 ML, respectively), making ΔV to increase. Moreover, Γ_2 increases more than Γ_1, from $\simeq$ 20.6 meV with 16 ML to $\simeq$ 25.1 meV and $\simeq$ 31.0 meV with 15 ML and 14 ML, respectively, because $d\Gamma_2/dt_b \gg d\Gamma_1/dt_b$ due to the lower electron confinement, which makes J_v to rise more than J_p. However, the impact of t_{qw} on both J_p and J_v is weaker with respect to t_b, as reported in Section IIA.

In summary, the analysis showed that, if J_p, ΔJ, and ΔV increase reducing t_{qw}, V_p rises and the PVCR drops [9] [10].

C. Lightly-doped spacers

1) Emitter spacer: the RES was simulated setting $t_{e,ls}$ = 50 nm and 100 nm, and $N_{De,ls} = 2\times10^{16}$ cm^{-3} and 2×10^{17} cm^{-3}, while the lightly-doped collector spacer thickness $t_{c,ls}$ and doping level $N_{Dc,ls}$ were set to 100 nm, and 2×10^{17} cm^{-3} and 2×10^{16} cm^{-3}, respectively. The computed static JV characteristics are shown in Fig. 5 and the associated values in Table III, which were $J_p \simeq$ 265 kA/cm^2, $V_p \simeq$ 1.20 V, and $\Delta V \simeq$ 1.54 V with $t_{e,ls}$ = 50 nm and $N_{De,ls} = 2\times10^{17}$ cm^{-3}, $J_p \simeq$ 265 kA/cm^2, $V_p \simeq$ 1.20 V, and $\Delta V \simeq$ 1.54 V with $t_{e,ls}$ = 100 nm and $N_{De,ls} = 2\times10^{17}$ cm^{-3}, $J_p \simeq$ 215 kA/cm^2, $V_p \simeq$ 1.08 V, and $\Delta V \simeq$ 1.66 V with $t_{e,ls}$ = 50 nm and $N_{De,ls} = 2\times10^{16}$ cm^{-3}, and $J_p \simeq$ 206 kA/cm^2, $V_p \simeq$ 1.04 V, and $\Delta V \simeq$ 1.70 V with $t_{e,ls}$ = 100 nm and $N_{De,ls} = 2\times10^{16}$ cm^{-3} assuming $t_{c,ls}$ = 100 nm and $N_{Dc,ls} = 2\times10^{17}$ cm^{-3}. Moreover, simulations gave $J_p \simeq$ 265 kA/cm^2, $V_p \simeq$ 2.28 V, and $\Delta V \simeq$ 1.76 V with $t_{e,ls}$ = 50 nm and $N_{De,ls} = 2\times10^{17}$ cm^{-3}, and $J_p \simeq$ 265 kA/cm^2, $V_p \simeq$ 2.28 V, and $\Delta V \simeq$ 1.76 V with $t_{e,ls}$ = 100 nm and $N_{De,ls} = 2\times10^{17}$ cm^{-3} assuming $t_{c,ls}$ = 100 nm and $N_{Dc,ls} = 2\times10^{16}$ cm^{-3}.

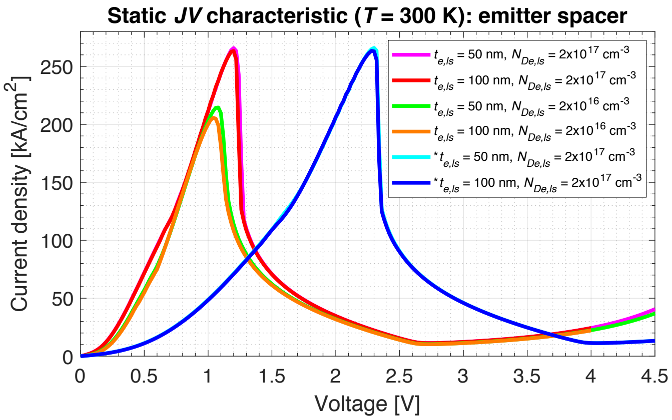

Fig. 5. Computed static JV characteristic at RT for different lightly-doped emitter spacer thicknesses $t_{e,ls}$ and doping levels $N_{De,ls}$. The lightly-doped collector spacer thickness $t_{c,ls}$ and doping level $N_{Dc,ls}$ were set to 100 nm and 2×10^{17} cm^{-3}, respectively. *Computed assuming $t_{c,ls}$ = 100 nm and $N_{Dc,ls} = 2\times10^{16}$ cm^{-3}.

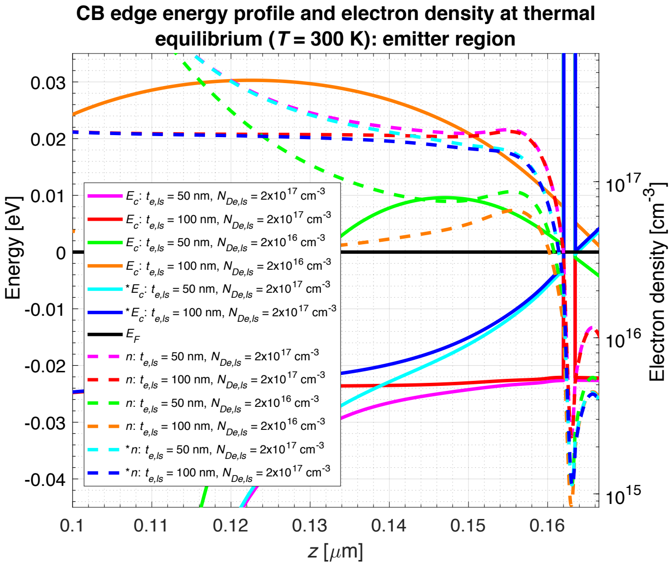

Fig. 6. Computed conduction band (CB) edge energy E_c profile and electron density n at RT and thermal equilibrium in the emitter region for different lightly-doped emitter spacer thicknesses $t_{e,ls}$ and doping levels $N_{De,ls}$. The lightly-doped collector spacer thickness $t_{c,ls}$ and doping level $N_{Dc,ls}$ were set to 100 nm and 2×10^{17} cm^{-3}, respectively. *Computed assuming $t_{c,ls}$ = 100 nm and $N_{Dc,ls} = 2\times10^{16}$ cm^{-3}. The black solid line represents the Fermi level E_F.

To compare and explain the results, the conduction band (CB) edge energy E_c profile (Γ point) and electron density n distribution in proximity to the first barrier at RT were computed, which are shown in Fig. 6. Thermal equilibrium was assumed to simplify the treatment. In the case of symmetric doping between emitter and collector lightly-doped spacers, no change in the JV characteristic was revealed when $t_{e,ls}$ was tuned, which can be explained by the weak variation in the potential barrier arising close to the QW at peak resonance, which was confirmed by the smoothness of E_c at thermal equilibrium. Similar considerations apply for the asymmetric case $N_{De,ls} > N_{Dc,ls}$, which was confirmed by the positive curvature of the potential profile in proximity to the first barrier at thermal equilibrium. On the other hand, if $N_{De,ls} < N_{Dc,ls}$, J_p drops with increasing $t_{e,ls}$, which can be explained by the larger potential barrier seen by the tunnelling electrons

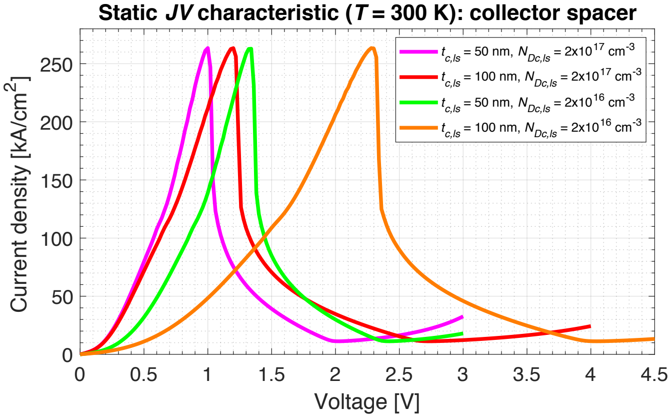

Fig. 7. Computed static JV characteristic at RT for different lightly-doped collector spacer thicknesses $t_{c,ls}$ and doping levels $N_{Dc,ls}$. The lightly-doped emitter spacer thickness $t_{e,ls}$ and doping level $N_{De,ls}$ were set to 100 nm and 2×10^{17} cm^{-3}, respectively.

TABLE III

SIMULATION RESULTS FOR DIFFERENT EMITTER AND COLLECTOR LIGHTLY-DOPED SPACERS THICKNESSES AND DOPING LEVELS

$t_{e,ls}$ [nm]	$N_{De,ls}$ [cm^{-3}]	J_p [kA/cm^2]	V_p [V]	V_v [V]	ΔV [V]
*50	2×10^{17}	265	1.20	2.74	1.54
*100	2×10^{17}	265	1.20	2.74	1.54
*50	2×10^{16}	215	1.08	2.74	1.66
*100	2×10^{16}	206	1.04	2.74	1.70
**50	2×10^{17}	265	2.28	4.04	1.76
**100	2×10^{17}	265	2.28	4.04	1.76
$t_{c,ls}$ [nm]	$N_{Dc,ls}$ [cm^{-3}]	J_p [kA/cm^2]	V_p [V]	V_v [V]	ΔV [V]
*50	2×10^{17}	265	1.00	2.02	1.02
*100	2×10^{17}	265	1.20	2.74	1.54
*50	2×10^{16}	265	1.34	2.42	1.08
*100	2×10^{16}	265	2.28	4.04	1.76

* Computed assuming $t_{c/e,ls} = 100$ nm and $N_{Dc/e,ls} = 2\times10^{17}$ cm^{-3}.
** Computed assuming $t_{c,ls} = 100$ nm and $N_{Dc,ls} = 2\times10^{16}$ cm^{-3}.

when the equivalent voltage drop across the depletion regions at the emitter side at $V = V_p$ is not enough to compensate for the associated intrinsic built-in potential, which is the case if the emitter contact is heavily doped (whose doping level was set to 2×10^{19} cm^{-3}). This was confirmed by the negative profile of the potential at thermal equilibrium. Moreover, J_p decreases if $N_{De,ls}$ is reduced due the lower available electron concentration, making E_c to shift towards and above the Fermi level E_F. In both cases, V_p decreases since E_c and E_1 get closer because of band warping caused by the larger potential drop at the emitter side, increasing ΔV. Generally speaking, both $J_p, V_p(t_{e,ls}, N_{De,ls})$ are expected to depend on Thomas-Fermi screening effects caused by charge accumulation close to the first barrier. Furthermore, V_v resulted to be unaffected by both $t_{e,ls}$ and $N_{De,ls}$, where the estimated V_v were $\simeq 2.74$ V and $\simeq 4.04$ V assuming $N_{Dc,ls} = 2\times10^{17}$ cm^{-3} and 2×10^{16} cm^{-3}, respectively. However, J_p, V_p, and V_v are expected to change as $t_{e,ls}$ increases and/or $N_{De,ls}$ decreases due to dissipative processes, which were not included in the simulations.

In summary, the analysis showed that, while J_p, V_p, and ΔV considerably change if $N_{De,ls}$ is tuned, their dependence on $t_{e,ls}$ turns to be relevant only if $N_{De,ls}/N_{De,ls} \lll 1$. In particular, both J_p and V_p decreases, while ΔV increases, if either $N_{De,ls}$ is reduced or $t_{e,ls}$ increased [8].

2) Collector spacer: the RES was simulated setting $t_{c,ls} =$ 50 nm and 100 nm, and $N_{Dc,ls} = 2\times10^{16}$ cm^{-3} and 2×10^{17} cm^{-3}, while the lightly-doped emitter spacer thickness $t_{e,ls}$ and doping level $N_{De,ls}$ were set to 100 nm and 2×10^{17} cm^{-3}, respectively. The computed static JV characteristics are shown in Fig. 7 and the associated values in Table III, which were $J_p \simeq 263$ kA/cm^2, $V_p \simeq 1.00$ V, $V_v \simeq 2.02$ V, and $\Delta V \simeq 1.02$ V with $t_{c,ls} = 50$ nm and $N_{Dc,ls} = 2\times10^{17}$ cm^{-3}, $J_p \simeq 263$ kA/cm^2, $V_p \simeq 1.20$ V, $V_v \simeq 2.74$ V, and $\Delta V \simeq 1.54$ V with $t_{c,ls} = 100$ nm and $N_{Dc,ls} = 2\times10^{17}$ cm^{-3}, $J_p \simeq 263$ kA/cm^2, $V_p \simeq 1.34$ V, $V_v \simeq 2.42$ V, and $\Delta V \simeq 1.08$ V with $t_{c,ls} = 50$ nm and $N_{Dc,ls} = 2\times10^{16}$ cm^{-3}, and $J_p \simeq 263$ kA/cm^2, $V_p \simeq 2.28$ V, $V_v \simeq 4.04$ V, and $\Delta V \simeq 1.76$ V with $t_{c,ls} = 100$ nm and $N_{Dc,ls} = 2\times10^{16}$ cm^{-3}. The shift of V_p and V_v at higher voltage if $t_{c,ls}$ is increased and/or $N_{Dc,ls}$ decreased is explained by the larger voltage drop across the collector region. In particular, V_v shifts more than V_p since the inequality $E_1 - E_c < E_2 - E_1$ is met, increasing ΔV. Generally speaking, both $V_p, V_v(t_{c,ls}, N_{Dc,ls})$ are expected to depend on the resistive nature of the collector depletion region of thickness l_{dc} through the ratio l_{dc}/L_{Dc}, where L_{Dc} is the associated Debye length. At the same time, J_p does not change by tuning both $t_{c,ls}$ and/or $N_{Dc,ls}$, where the computed J_p was $\simeq 265$ kA/cm^2, unless a large potential barrier approaching E_1 arises in proximity to the second barrier at $V = V_p$ if $N_{Dc,ls} \lll N_{De,ls}$. However, it is expected J_p, V_p, and V_v to change as $t_{c,ls}$ increases and/or $N_{Dc,ls}$ decreases due to inelastic scattering mechanisms.

In summary, the analysis showed that both V_p and ΔV increase if $t_{c,ls}$ is increased and/or $N_{Dc,ls}$ is decreased, while J_p is unaffected if scattering is neglected [9] [11].

D. High-bandgap emitter

The impact of a high energy bandgap E_g material employed at the emitter side was investigated. A quaternary $\mathrm{In}_{1-x-y}\mathrm{Al}_y\mathrm{Ga}_x\mathrm{As}$ compound was assumed [11]. To show that, the RES was simulated setting $t_{qw} = 4.10$ nm and assuming different alloy compositions $\{x, y\} = \{0.43, 0.04\}$ ($E_g \simeq 0.93$ eV), $\{0.4, 0.07\}$ ($E_g \simeq 0.98$ eV), and $\{0.37, 0.1\}$ ($E_g \simeq 1.04$ eV) [12]. Simulations results are shown in Table IV, revealing a drop of V_p with increasing the aluminium (Al) concentration, where computed values were $V_p \simeq 0.84$ V, $\simeq 0.66$ V, and $\simeq 0.52$ V with $\{x, y\} = \{0.43, 0.04\}$, $\{0.4, 0.07\}$, and $\{0.37, 0.1\}$, respectively, reducing V_p up to ~ 3 times if compared to an equivalent heterostructure employing

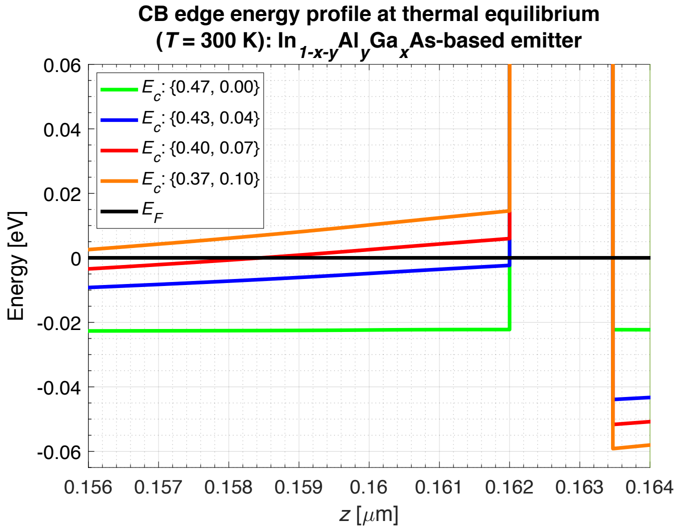

Fig. 8. Computed CB edge energy E_c profile at RT and thermal equilibrium in proximity to the first barrier for different $\mathrm{In}_{1-x-y}\mathrm{Al}_y\mathrm{Ga}_x\mathrm{As}$ compositions. The black solid line represents the Fermi level E_F.

TABLE IV
SIMULATION RESULTS FOR DIFFERENT EMITTER ALLOYS

Compound	J_p [kA/cm^2]	V_p [V]
$\mathrm{In}_{0.53}\mathrm{Ga}_{0.47}\mathrm{As}$	338	1.44
$\mathrm{In}_{0.53}\mathrm{Al}_{0.04}\mathrm{Ga}_{0.43}\mathrm{As}$	220	0.84
$\mathrm{In}_{0.53}\mathrm{Al}_{0.07}\mathrm{Ga}_{0.4}\mathrm{As}$	180	0.66
$\mathrm{In}_{0.53}\mathrm{Al}_{0.1}\mathrm{Ga}_{0.37}\mathrm{As}$	145	0.52

$\mathrm{In}_{0.53}\mathrm{Ga}_{0.47}\mathrm{As}$ ($E_g \simeq 0.74$ eV [13]), whose V_p was estimated to be $\simeq$ 1.44 V. At the same time, J_p drops, where computed values decrease from $\simeq$ 338 kA/cm^2 with $y = 0$ to $J_p \simeq 220$ kA/cm^2, $\simeq$ 180 kA/cm^2, and $\simeq$ 145 kA/cm^2, with $\{x, y\} = \{0.43, 0.04\}$, $\{0.4, 0.07\}$, and $\{0.37, 0.1\}$, respectively.
To explain the results, the E_c profile at RT close to the first barrier was analysed, which is shown in Fig. 8. Thermal equilibrium was assumed to simplify the treatment. As it is possible to see, the drop of V_p can be explained by the shift of E_c in both emitter and QW regions, which makes E_c and E_1 to approach. However, J_p drops at the same time mainly due to the higher electron effective mass m_e^* of $\mathrm{In}_{1-x-y}\mathrm{Al}_y\mathrm{Ga}_x\mathrm{As}$ ($0.047 \lesssim m_e^* \lesssim 0.053$) compared to $\mathrm{In}_{0.53}\mathrm{Ga}_{0.47}\mathrm{As}$ ($m_e^* \sim 0.041$) [12].
In summary, the analysis showed that the employment of a high-bandgap emitter region lowers both V_p and J_p [11].

III. CONCLUSIONS

In this work, we studied the impact of barriers, QW, and spacer layers design of $\mathrm{In}_{0.53}\mathrm{Ga}_{0.47}\mathrm{As}$/AlAs RTD heterostructures on the associated static JV characteristic by employing a NEGF-based quantum transport simulator. We observed that while barriers and QW thicknesses mostly control the current density operation of the RTD device, accurate asymmetric spacer layers design can compromise between the NDR region voltage span and relative position. Based on these considerations, future work will consist in optimising the RTD epitaxial structure design in order to improve the associated RF power performance in the low-THz band ($\sim$ 100−300 GHz).

IV. ACKNOWLEDGMENTS

The work of Davide Cimbri was supported by TeraApps (Doctoral Training Network in Terahertz Technologies for Imaging, Radar and Communication Applications), which received funding from the European Union's Horizon 2020 research and innovation programme under Marie Skłodowska-Curie Innovative Training Network (ITN) grant agreement No. 765426.

REFERENCES

[1] M. Feiginov, "Frequency Limitations of Resonant-Tunnelling Diodes in Sub-THz and THz Oscillators and Detectors," *Journal of Infrared, Millimeter, and Terahertz Waves*, vol. 40, no. 4, pp. 365-394, 2019, doi: 10.1007/s10762-019-00573-5.

[2] T. Nagatsuma, "Terahertz technologies: present and future," *IEICE Electronics Express*, vol. 8, no. 14, pp. 1127-1142, 2011, doi: 10.1587/elex.8.1127.

[3] R. Izumi, S. Suzuki, and M. Asada, "1.98 THz resonant-tunneling-diode oscillator with reduced conduction loss by thick antenna electrode," *42nd International Conference on Infrared, Millimeter, and Terahertz Waves (IRMMW-THz)*, pp. 1-2, 2017, doi: 10.1109/IRMMW-THz.2017.8066877.

[4] D. Cimbri, J. Wang, A. Al-Khalidi, and E. Wasige, "Resonant Tunnelling Diode High-Speed Terahertz Wireless Communications - A Review," *IEEE Transactions on Terahertz Science and Technology*, vol. 12, no. 3, pag. 226-244, 2022, doi: 10.1109/TTHZ.2022.3142965.

[5] H. -J. Song and T. Nagatsuma, "Present and Future of Terahertz Communications," *IEEE Transactions on Terahertz Science and Technology*, vol. 1, no. 1, pp. 256-263, 2011, doi: 10.1109/TTHZ.2011.2159552.

[6] D. Cimbri, B. Yavas-Aydin, F. Jabeen, L. Worschech, S. Höfling, and E. Wasige, "Accurate Quantum Transport Modelling of High-Speed $\mathrm{In}_{0.53}\mathrm{Ga}_{0.47}\mathrm{As}$/AlAs Double-Barrier Resonant Tunnelling Diodes," *IEEE Transactions on Electron Devices* (in review).

[7] A. Al-Khalidi, K. H. Alharbi, J. Wang, R. Morariu, L. Wang, A. Khalid, J. M. L. Figueiredo, and E. Wasige, "Resonant Tunneling Diode Terahertz Sources With up to 1 mW Output Power in the J-Band," *IEEE Transactions on Terahertz Science and Technology*, vol. 10, no. 2, pp. 150-157, 2020, doi: 10.1109/TTHZ.2019.2959210.

[8] H. Sugiyama, H. Yokoyama, A. Teranishi, S. Suzuki, and M. Asada, "Extremely High Peak Current Densities of over 1×10^6 A/cm^2 in InP-Based InGaAs/AlAs Resonant Tunneling Diodes Grown by Metal-Organic Vapor-Phase Epitaxy," *Japanese Journal of Applied Physics*, vol. 49, no. 5, pp. 051201, 2010, doi: 10.1143/jjap.49.051201.

[9] H. Kanaya, T. Maekawa, S. Suzuki, and M. Asada, "Structure dependence of oscillation characteristics of resonant-tunneling-diode terahertz oscillators associated with intrinsic and extrinsic delay times," *Japanese Journal of Applied Physics*, vol. 54, no. 9, pp. 094103, 2015, doi: 10.7567/jjap.54.094103.

[10] H. Kanaya, H. Shibayama, R. Sogabe, S. Suzuki, and M. Asada, "Fundamental Oscillation up to 1.31 THz in Resonant Tunneling Diodes with Thin Well and Barriers," *Applied Physics Express*, vol. 5, no. 12, pp. 124101, 2012, doi: 10.1143/apex.5.124101.

[11] H. Kanaya, R. Sogabe, T. Maekawa, S. Suzuki, and M. Asada, "Fundamental Oscillation up to 1.42 THz in Resonant Tunneling Diodes by Optimized Collector Spacer Thickness," *Journal of Infrared, Millimeter, and Terahertz Waves*, vol. 35, no. 5, pp. 425-431, 2014, doi: 10.1007/s10762-014-0058-z.

[12] S. L. Chuang, "Physics of Optoelectronic Devices," *Wiley*, 1995.

[13] M. Levinshtein, S. Rumyantsev, and M. Shur, "Handbook Series on Semiconductor Parameters: Volume 1 and 2," *World Scientific*, 1996, doi: 10.1142/2046.